Materials Today Bio 16 (2022) 100366

Contents lists available at ScienceDirect

Materials Today Bio

journal homepage: www.journals.elsevier.com/materials-today-bio

J-aggregates albumin-based NIR-II fluorescent dye nanoparticles for cancer phototheranostics

Bulin Du [a,d,1], Ruiqi Liu [e,1], Chunrong Qu [d], Kun Qian [d], Yongkuan Suo [e], Fengxia Wu [e], Hongda Chen [f], Xuena Li [a], Yaming Li [a,**], Hongguang Liu [e,***], Zhen Cheng [b,c,d,*]

[a] Department of Nuclear Medicine, The First Hospital of China Medical University, Shenyang, 110001, China
[b] State Key Laboratory of Drug Research, Molecular Imaging Center, Shanghai Institute of Materia Medica, Chinese Academy of Sciences, Shanghai, 201203, China
[c] Shandong Laboratory of Yantai Drug Discovery, Bohai Rim Advanced Research Institute for Drug Discovery, Yantai, 264000, China
[d] Molecular Imaging Program at Stanford (MIPS), Canary Center at Stanford for Cancer Early Detection, Department of Radiology and Bio-X Program, School of Medicine, Stanford University, California, 94305-5484, USA
[e] Institute of Molecular Medicine, College of Life and Health Sciences, Northeastern University, Shenyang, 110000, China
[f] Changchun Institute of Applied Chemistry, Chinese Academy of Science, Changchun, 130000, China

ARTICLE INFO

Keywords:
IR1061
Human serum albumin
Nanoparticles
Second near-infrared window
Fluorescence imaging
Photothermal therapy

ABSTRACT

Phototheranostics, relying on energy conversions of fluorophores upon excitation, integrating diagnostic fluorescence imaging and photo-driven therapy, represents a promising strategy for cancer precision medicine. Compared with the first near-infrared biological window (NIR-I), fluorophores imaged in the second window (NIR-II, 1000–1700 nm) exhibit a higher temporal and spatial resolution and tissue penetration depth. Polymethine cyanine-based dye IR1061 is a typical NIR-II small-molecule organic fluorophore, but its low water solubility and short circulation time limiting its biological applications. Therefore, human serum albumin (HSA) nanoparticles with great biocompatibility and biosafety were employed to fabricate hydrophobic IR1061, which exhibited red-shifted absorption band as typical for J-aggregates. Moreover, IR1061@HSA nanoparticles can be successfully used for NIR-II imaging to noninvasively visualize the tumor vascular networks, as well as real-time intraoperative image-guided tumor resection. Interestingly, benefiting from the high photothermal conversion efficiency brought by J-aggregates, IR1061@HSA nanoparticles were also explored for photothermal therapy (PTT) and cause efficient thermal ablation of tumors. Overall, IR1061@HSA, as a novel J-aggregates albumin-based NIR II dye nanoparticle with high biocompatibility, provides an integrated versatile platform for cancer phototheranostics with promising clinical translation prospects.

1. Introduction

Cancer is the leading cause of death, and the global burden of cancer morbidity and mortality is growing rapidly [1]. The development of effective cancer diagnostic and therapeutic tools is urgently required. An exciting area of combining diagnosis and treatment of cancer into a single theranostic platform has attracted tremendous attention [2]. Phototheranostics, relying on energy conversions of fluorophores upon excitation, integrating diagnostic fluorescence imaging (FLI) and photodynamic and/or photothermal therapy (PDT, PTT), represents a promising strategy in early diagnosis and precision treatment of cancers [3,4]. FLI for surgical navigation can reliably assist for the tumor resection in real-time, and further photo-driven therapy enables ablation of potentially invisible lesions. Therefore, the development of ideal fluorophores is critical for cancer phototheranostics.

Small-molecule organic fluorophores with great biocompatibility have proven to be attractive candidates for clinical phototheranostics [5]. Compared with the first near-infrared biological window (NIR-I),

* Corresponding author. Molecular Imaging Center, Shanghai Institute of Materia Medica, Chinese Academy of Sciences, 647 Songtao Road, Building 3, 4th floor, Pudong District, Shanghai, Zip code: 201203, China.
** Corresponding author. Department of Nuclear Medicine, The First Hospital of China Medical University, No.155, North Nanjing Street, Heping District, Shenyang. Zip code: 110001, China.
*** Corresponding author. Institute of Molecular Medicine, College of Life and Health Sciences, Northeastern University, Shenyang, Zip code: 110000, China.
E-mail addresses: ymli2001@163.com (Y. Li), simonliu@mail.neu.edu.cn (H. Liu), zcheng@simm.ac.cn (Z. Cheng).
[1] These authors contributed equally to this work.

https://doi.org/10.1016/j.mtbio.2022.100366
Received 22 May 2022; Received in revised form 13 July 2022; Accepted 13 July 2022
Available online 7 August 2022

fluorophores imaged in the second window (NIR-II, 1000–1700 nm) exhibit a higher temporal and spatial resolution and tissue penetration depth [6–11]. Polymethine cyanine-based dye IR1061 (λem = 1061 nm in methylene chloride) is a typical small-molecule organic fluorophore whose emission wavelength is in the NIR-II window, which is composed of two heterocyclic terminal groups connected by the polymethine linker [12]. Although it is commercially available, low water solubility and short circulation time limiting its biological applications [13]. In order to improve its biomedical applications, the hydrophobic dye has been fabricated into a variety of platforms such as polymers [14,15], lipid [16] and nanoprobe [17,18] for *in vivo* imaging or therapeutic applications. However, many crucial hurdles including biological safety and complexity of production and formulation remain to be resolved, to render IR1061 based agents clinical translatable.

Human serum albumin (HSA) is a plasma protein rich in human body. Due to its obvious advantages such as high biocompatibility, high stability and ease of preparation, it plays an important role as a multifunctional drug nanocarrier [19–21]. Moreover, HSA can accumulate in tumor interstitium and be taken up by tumor cells through micropinocytosis [22]. In addition, compared to free HSA, due to longer lifetime in blood circulation, the enhanced permeability and retention effect (EPR) and secreted protein acidic and rich in cysteine (SPARC) [23], appropriately sized HSA nanoparticles tend to accumulate in the tumor more efficiently [19]. All these findings have motivated scientists to extensively explore HSA as a drug carrier for cancer imaging or therapy [24,25]. Although HSA has been used to form complexes with hydrophilic organic dyes to increase the brightness by restricting the intramolecular rotation of the fluorophore [26–28], it is not suitable for hydrophobic dyes. Based on the strategy of albumin-based drug carriers for poorly water-soluble drugs [29–31], HSA nanoparticles are assumed to be a novel way to fabricate hydrophobic IR1061 to improve the feasibility of clinical translation, thereby exploiting its advantages in cancer theranostics.

Herein, a novel albumin-NIR II dye nanoparticles IR1061@HSA was constructed, which was supposed to be effectively used for tumor NIR-II imaging and intraoperative NIR-II image-guided tumor resection. Furthermore, benefiting from the high photothermal conversion efficiency brought by J-aggregates of IR1061 arranged in the nanoparticles, IR1061@HSA nanoparticles were also investigated for application in PTT, which uses NIR-absorbing photothermal substance to convert NIR light into heat for tumor ablation [19,32,33]. Overall, a multifunctional NIR-II cancer phototheranostic platform was constructed from HSA-based nanoparticles (Scheme 1), which may expand the anticancer arsenal and holds promise for cancer theranostics.

2. Material and methods

2.1. Materials

HSA was purchased from EMD Millipore (Billerica, MA, USA). IR1061 dye and methanol were purchased from Sigma-Aldrich (St. Louis., MO, USA). All reagents and solvents were of analytical grade and used without further purification.

2.2. Synthesis of IR1061@HSA nanoparticles and molecular modeling

IR1061@HSA nanoparticles were prepared using the desolvation and thermal denaturation method [34–36]. Briefly, IR1061 (0.15 mg) was first dispersed in 3 mL of methanol. The solution was then added dropwise to 26.4 mg HSA dispersed in 3 mL of DI water with stirring at room temperature. Subsequently, denaturation by heating was employed. The obtained mixture was heated at temperature 80 °C for 2 h. The reactant was transferred into centrifuge tubes and dried in a vacuum centrifuge concentrator (Jiaimu CV200, Beijing, China). The nanoparticles were then redispersed in an ultrasonication bath [37]. The concentration of IR1061@ HSA nanoparticles was based on IR1061.

The absorbance of the IR1061 in methanol at various concentrations was measured and used to fit the equation of concentration and absorbance. Since IR1061 is insoluble in the water, the unloaded IR1061 in dispersions was extracted with dichloromethane and then dissolved in the methanol after evaporation of the solvent. The absorbance of the extracted IR1061 was obtained, and the amount was calculated according to the acquired equation. Finally, the IR1061 encapsulation efficiency was calculated [16].

IR1061 and the crystal structure of HSA was first prepared using Sybyl-X software (Tripos Inc., MO, USA). A Surflex Dock package was utilized for molecular docking, the parameters were as follows: additional starting conformation per molecule, 20; max conformation per fragment, 20; Angstroms to expand search grid, 6; max number of rotatable bonds per molecule, 100.

2.3. Characterization and photostability of IR1061@HSA nanoparticles

The morphology of IR1061@HSA nanoparticles were analyzed by using a JEM-2100 transmission electron microscope (JEOL Ltd, Tokyo, Japan) with an acceleration voltage of 200 kV. The zeta potential and the hydrodynamic particle size distribution of IR1061@HSA nanoparticles were determined using a Malvern Mastersizer 2000 (Malvern Instruments Ltd, Malvern, UK). Absorbance spectra of IR1061 in methanol

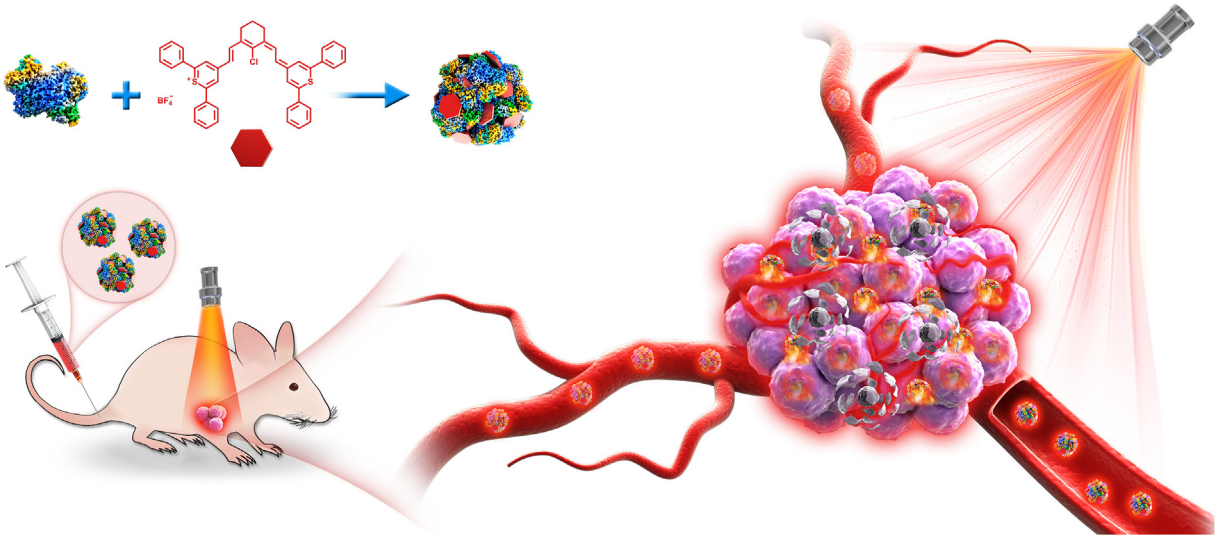

Scheme 1. Schematic illustration of IR1061@HSA nanoparticles for tumor biomedical imaging including surgical navigation in the NIR-II window and PTT.

and IR1061@HSA nanoparticles dispersed in aqueous solutions were recorded on an ultraviolet-visible-NIR UV-3101PC spectrometer (Shimadzu, Kyoto, Japan). The NIR-II fluorescence spectra were collected on an in-house built system consisting of a cuvette holder (Thorlabs, Newton, NJ, USA) for micro and macro cuvettes, a SMA905 fiber adapter, an 808 nm laser (Changchun Laser Technology, Changchun, China), two plano-convex lens (Thorlabs), a long-pass filter (Thorlabs), a bandpass filter (Thorlabs), and a NIR spectrometer (Ocean Optics, Dunedin, FL, USA) covering 900–1700 nm.

The NIR-II fluorescence quantum yield of the IR1061@HSA nanoparticles was measured following the procedure described previously [38]. Briefly, IR26 was used as a reference fluorophore (QY = 0.5%). Different concentrations of IR26 solutions and IR1061@HSA nanoparticles dispersions with an OD < 0.1 at 808 nm were prepared, and then the absorbance at 808 nm and the fluorescent intensity values were measured. The quantum yield was calculated according to the previously reported equation [38].

To investigate the photostability of IR1061@HSA nanoparticles in an aqueous solution, the fluorescence intensity of IR1061@HSA nanoparticles (400 μM, 500 μL) in DI water were measured when exposed to continuous illumination at 808 nm (QPC Lasers Inc., Sylmar, CA, USA) for 60 min. To prepare the photobleaching curves, the data was normalized by dividing the fluorescence intensity of each time point by the fluorescence intensity at t = 0.

2.4. Photothermal effects of IR1061@HSA nanoparticles

The photothermal therapy experiments were conducted using an 808 nm laser. The thermal images and temperatures were recorded every minute using an infrared thermal imager (FLIR, Nashua, NH, USA). The 808 nm laser (1 W/cm^2) was used to irradiate the aqueous solution of IR1061@HSA nanoparticles at different concentrations (400, 200, 100, 50, and 20 μM) for 15 min. PBS was used as a control.

For anti-photobleaching studies, the temperatures of the sample solutions were collected during three heating and cooling cycles. In the cycle, the temperature change of IR1061@HSA nanoparticle dispersion was recorded over time until the solution reaches the steady-state temperature under the continuous laser irradiation (808 nm, 1 W/cm^2), then turn off the laser until the temperature naturally reaches ambient temperature. Three irradiation cycles were performed to study the photothermal stability of the IR1061@HSA nanoparticles (400 μM).

The photothermal conversion efficiency (PCE) was determined by recording the temperature change of the IR1061@HSA nanoparticles dispersions under the continuous laser irradiation (808 nm, 1 W/cm^2) for 10 min, the laser was then turned off until the temperature reached the ambient temperature. The PCE was calculated according to previously reported equation [39].

2.5. Biocompatibility and cytotoxicity experiments in vitro

Human bone osteosarcoma (143B) and mouse embryonic fibroblasts (NIH-3T3) cell lines were obtained from the American Type Culture Collection (ATCC, Manassas, VA, USA) and cultured in Dulbecco's modified Eagle medium (DMEM) containing 10% FBS, 100 IU/mL penicillin, 100 μg/mL streptomycin at 37 °C with 5% CO_2 atmosphere.

The potential cytotoxicity of IR1061@HSA nanoparticles on NIH3T3 and 143B cells was assessed using a standard MTT (Sigma-Aldrich, St. Louis., MO, USA) assay. NIH3T3 or 143B cells (1×10^4 cells per well) were first seeded in 96-well plates and incubated for 24 h. The medium was then replaced with medium containing IR1061@HSA nanoparticles at different concentrations (0, 10, 20, 40, and 80 μM). After 24 h, the MTT (10 μL, 5 mg/mL) solution was added and incubated for 4 h. After the supernatant was removed, dimethyl sulfoxide (200 μL) was used to dissolve the crystals. The absorbance was measured at 490 nm using a microplate reader (Tecan, Männedorf, Switzerland). The relative cell viability (%) was calculated using the equation, $(A_{sample}/A_{blank}) \times 100\%$. The experiments were replicated three times.

For photothermal therapy studies, 143B cells seeded in 96-well plates were incubated with IR1061@HSA nanoparticles at different concentrations (0, 10, 20, 40, 60 and 80 μM) for 4 h, and then irradiated with 808 nm laser (1 W/cm^2) for 5 min per well. The control group was incubated with IR1061@HSA nanoparticles at the same concentrations without laser irradiation. After removing the medium, the plate was washed with PBS. Then, perform the standard MTT method to measure cell viability, as above. The experiments were replicated three times.

2.6. In vivo animal NIR-II imaging

All animal experiments were performed under the approval of Stanford University's Administrative Panel on Laboratory Animal Care. Six-week-old female BALB/c nude mice were used in all imaging studies and housed at the Research Animal Facility under our approved animal protocols. Approximately 2×10^6 143B cells in DMEM media (no FBS) were hypodermically injected into the left shoulder of the nude mice. All the 143B osteosarcoma tumor-bearing mice were anesthetized before imaging. For vascular system and tumor imaging, IR1061@HSA nanoparticles (100 μL, 400 μM) and PBS (100 μL) were mixed and then intravenously injected with the mice in the supine position under anesthesia.

All NIR-II images were captured on a two-dimensional InGaAs array NIR-II system (Princeton Instruments, Trenton, NJ, USA). Fluorescence emission was collected with 1000 nm or >1000 nm long-pass filters (Thorlabs) under excitation provided by an 808 nm diode laser.

2.7. NIR-II image-guided PTT in vivo

To evaluate the photothermal effect of the IR1061@HSA nanoparticles *in vivo*, the 143B osteosarcoma tumor-bearing mice (n = 5) were intravenously injected with PBS mixed IR1061@HSA nanoparticles (200 μM, 200 μL) or PBS (200 μL). After 4 h, the mice were then irradiated with 808 nm wavelength laser (1 W/cm^2, 5 min). The temperature changes and IR images were recorded at different time points in 5 min using an infrared thermal imager. The tumor size and body weight were recorded each day. Using the equation to calculate the tumor volume: tumor volume = width^2 × length/2. All mice were sacrificed on day 15 after PTT, and the tumor tissues were excised for further analysis.

2.8. H&E staining

The harvested major organs and tumor tissues were fixed with 4% paraformaldehyde overnight. Then, these organs and tissues were embedded in optimal cutting temperature compound, cut into 5 μm slices with a microtome in the cryostat at −20 °C, and then transferred onto microscope slides for H&E staining (Solarbio, Beijing, China). The stained sections were imaged (Olympus, Tokyo, Japan).

2.9. Statistical analysis

The fluorescence measurement was performed to quantify the NIR-II fluorescence signal intensity using the ImageJ software (National Institutes of Health, Bethesda, MD, USA). The line graphs and Gaussian-fitted full width at half maximum (FWHM) were analyzed with Origin 8.5 (OriginLab Corporation, Northampton, MA, USA) and GraphPad Prism 6 (GraphPad Software, San Diego, CA, USA).

3. Results and discussion

3.1. Synthesis of IR1061@HSA nanoparticles and molecular modeling

IR1061 was first dissolved in methanol, and then it was added to an equal volume of HSA aqueous solution with an IR1061 to HSA molar ratio of 1:2. Heating time was explored at 80 °C, and 2 h was determined

to be the optimum time (Fig. S1). Sybyl-X software docking results showed that IR1061 binds to subdomain IIA of HSA (Fig. S2a). IR1061 was much closer to hydrophobic residues of HSA (Fig. S2b). Hence, IR1061 was enclosed in the center of the nanoparticles, while the hydrophilic parts were exposed the outside. The encapsulation efficiency of IR1061@HSA nanoparticles was 96.33%. To achieve large-scale production of IR1061@HSA nanoparticles for future clinical translation, nanoparticle albumin-bound (nab) technology, an industrially applicable preparation method for the production of albumin-based drug carriers for poorly water-soluble drugs, can be employed [29–31].

3.2. Characterization of IR1061@HSA nanoparticles

The morphology of the IR1061@HSA nanoparticles was observed by transmission electron microscopy (TEM), as shown in Fig. 1a. The nanoparticles were uniformly dispersed in an aqueous solution with a diameter of 11–16 nm and a smooth surface in the TEM image. The hydrodynamic particle size distribution of IR1061@HSA nanoparticles was about 50 nm (Fig. 1b) with good stability (Fig. S3a). The zeta potential was about −44.7. Methanol used as a desolvent can produce very small spherical HSA nanoparticles. The particle size mainly depended on the amount of desolvating agent added [40]. The heat denaturation

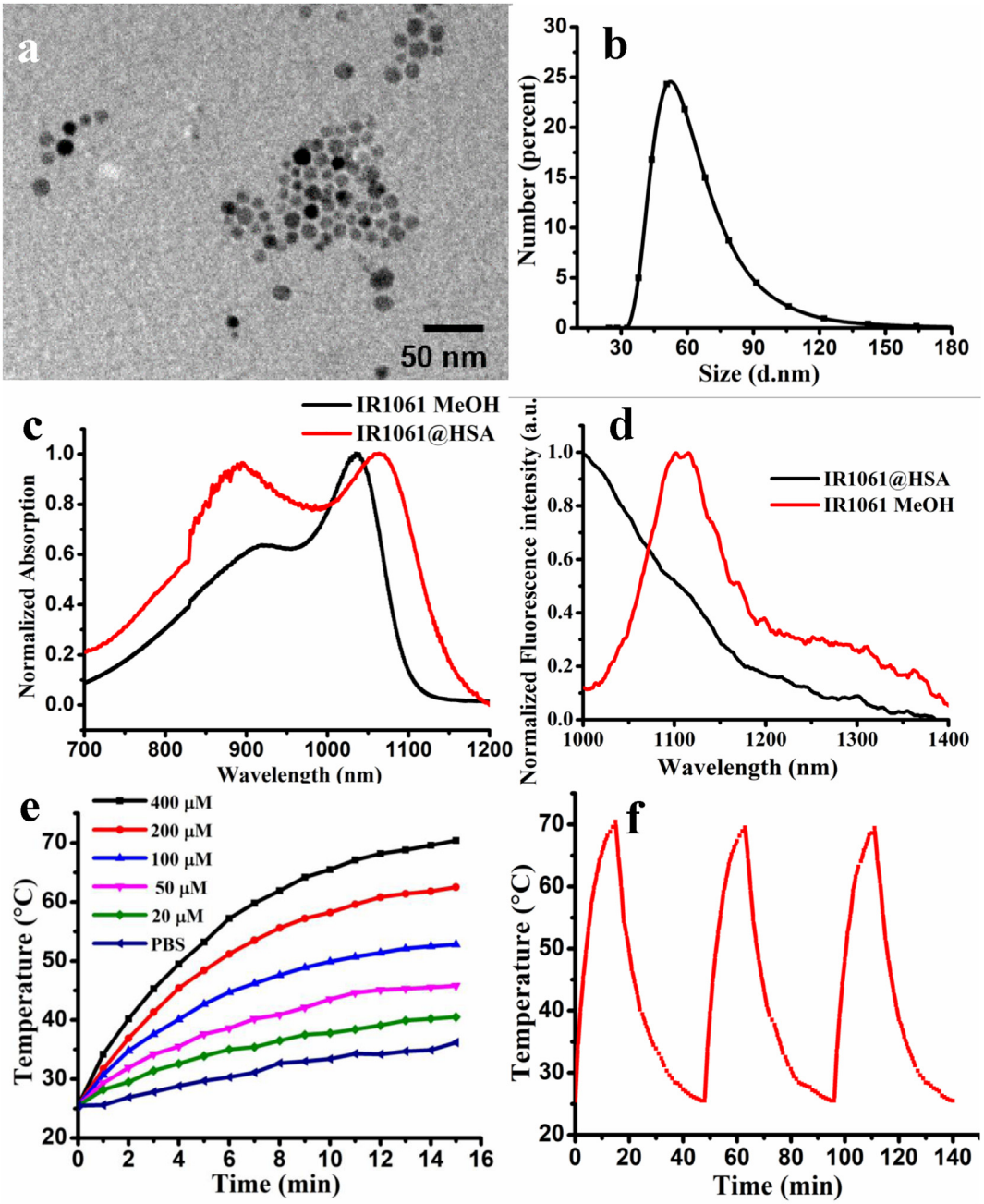

Fig. 1. Characteristics of IR1061@HSA nanoparticles. (a) Morphology and size of IR1061@HSA nanoparticles determined by TEM. Scale bar: 50 nm. (b) Hydrodynamic size of IR1061@HSA nanoparticles measured by dynamic light scattering. (c) Absorption spectrum of IR1061 in methanol and IR1061@HSA nanoparticles in DI water. (d) Fluorescence emission spectrum of IR1061 in methanol and IR1061@HSA nanoparticles in DI water after excitation with an 808 nm laser. (e) Temperature changes of IR1061@HSA nanoparticles at various concentrations (808 nm, 1 W/cm^2) in DI water. (f) Reliability of the photothermal conversion effect of IR1061@HSA nanoparticles during three cycles of heating-cooling (400 μM, 808 nm, 1 W/cm^2).

influenced the stability of the nanoparticles and the number of amino groups on the surface of the nanoparticles [41].

The absorption curve and fluorescent emission spectra of IR1061@HSA nanoparticles in deionized (DI) water were also assessed. The free IR1061 dye in methanol exhibited a strong peak at 1039 nm with a shoulder of 931 nm, while the nanoparticles exhibited a broader

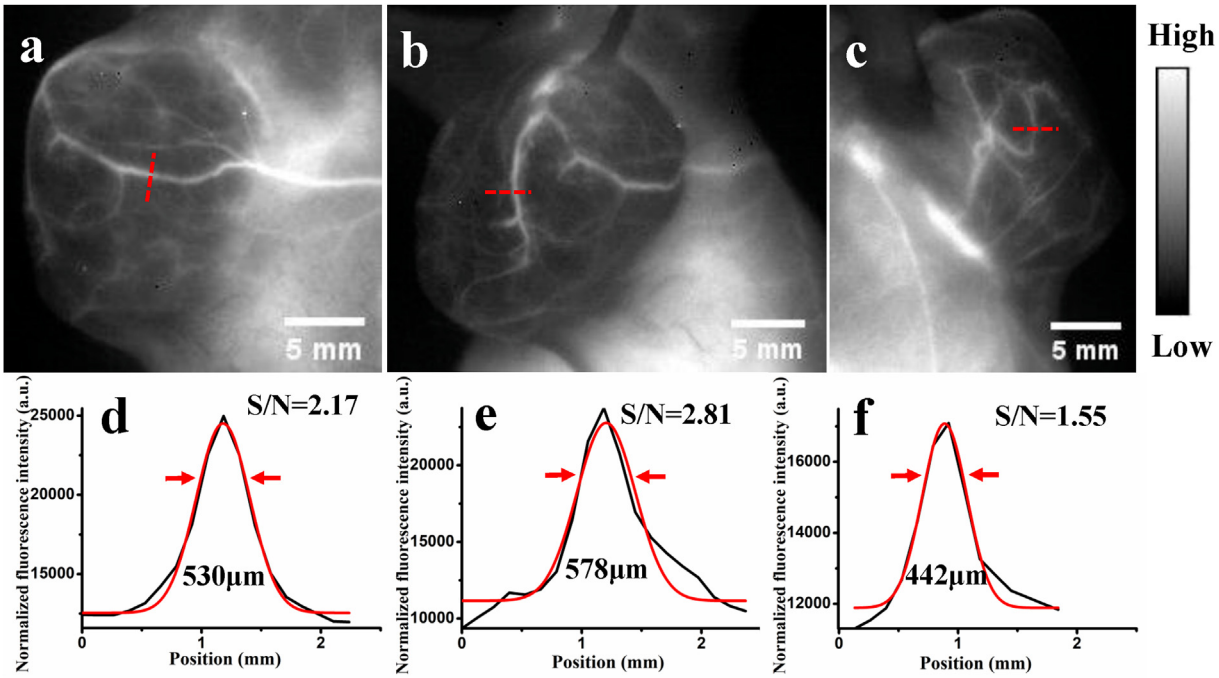

Fig. 2. NIR-II imaging blood supply network of the tumor. (a–c) NIR-II fluorescence images were taken from multiple angles with 143B osteosarcoma tumor-bearing mice in a lateral position after injection of IR1061@HSA nanoparticles. (d–f) FWHM values and SNRs of the tumor blood vessels (a red dash line in a-c) were analyzed based on the cross-sectional intensity profiles. Scale bar: 5 mm. (For interpretation of the references to color in this figure legend, the reader is referred to the Web version of this article.)

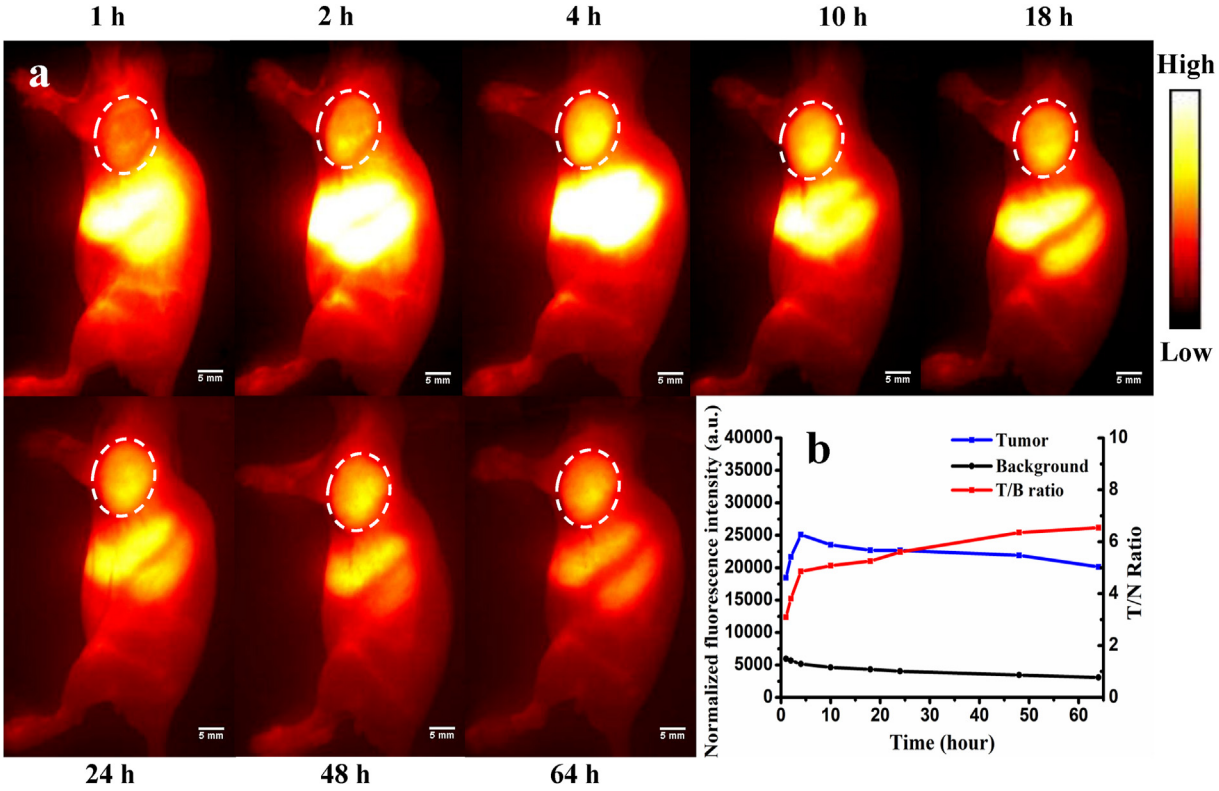

Fig. 3. NIR-II imaging of osteosarcoma with IR1061@HSA nanoparticles. (a) NIR-II images (1000 ms, 1000 LP) of 143B osteosarcoma tumor-bearing nude mice were taken at multiple time points from 1 h to 64 h after intravenously injection of IR1061@HSA nanoparticles. (b) Time-signal intensity curve of the tumor, background, and tumor-to-background ratios based on images shown in (a).

spectrum with absorbance peaks at 896 nm and 1060 nm (Fig. 1c). The emission of IR1061@HSA nanoparticles showed a blue-shift in the NIR-II window, compared with free IR1061 in methanol (Fig. 1d). The quantum yield of the IR1061@HSA nanoparticles was 1.15%. The altered absorption and emission spectrum indicating that the arrangement of IR1061 was transformed into the orderly J-aggregate form in nanoparticles [42–44]. Red-shift is primarily governed by short-range orbital interactions among IR1061 [45]. In addition to serving as an approach to prepare biocompatible NIR-II fluorophores [44], J-aggregates can also bring striking photothermal performance with favorable photostability and high conversion efficiency [46]. The IR1061@HSA nanoparticles in DI water exhibited excellent photostability when exposed to the 808 nm laser (Fig. S3b). Excellent photostability guarantees the potential of the IR1061@HSA nanoparticles for NIR-II bioimaging as well as other biological application.

Using HSA as the dye carrier, complexes were reported from our group on tailoring albumin with sulfonated NIR-II organic dyes (CH-4T) to dramatically increase fluorescence by 110-fold, resulting in molecular fluorophores with excellent quantum yield for NIR II imaging [27]. The fluorescence of NIR-I organic dye (IR820) complexes increased by an amazing 21 times, broadening its application in NIR-II imaging [26]. Herein, novel albumin-NIR-II dye nanoparticles IR1061@HSA that satisfies the essential characteristics seem to be qualified for NIR-II imaging.

3.3. Photothermal effects of IR1061@HSA nanoparticles in vitro

To verify the photothermal effect of IR1061@HSA nanoparticles, IR1061@HSA nanoparticles dispersions at different concentrations were exposed to 808 nm wavelength laser irradiation at a power density of 1 W/cm^2 for 15 min. As shown in Fig. 1e, only a slight temperature increase to 36 °C for PBS was seen, while the temperature of IR1061@HSA nanoparticles rose to 45–70 °C within 15 min for concentrations from 50 to 400 μM, which were sufficed for tumor photothermal treatment. Moreover, the photothermal conversion effect of the IR1061@HSA nanoparticles remained nearly unchanged with multiple times laser irradiations (Fig. 1f). Based on the temperature curve (Fig. S4), the calculated PCE was 51.89%. These characteristics indicate that IR1061@HSA nanoparticle is also a promising PTT nanoagent.

3.4. Biocompatibility and cytotoxicity experiments in vitro

To study the potential cytotoxicity of IR1061@HSA nanoparticles, standard cell viability assays were carried out. A cell viability test with NIH-3T3 and 143B tumor cell revealed no obvious cytotoxicity of IR1061@HSA nanoparticles, even at high HSA concentrations up to 80 μM (Fig. S5a). Next, using the tumor cells incubated with only IR1061@HSA nanoparticles as the control group, the viabilities of cells with IR1061@HSA nanoparticles combined with NIR laser treatment (808 nm, 1 W/cm^2, 5 min) were studied. As shown in Fig. S5b, as the concentration of IR1061@HSA nanoparticles increased, the cell viability of the control group remained mostly unchanged, while the viability of cells treated with nanoparticles and the laser gradually decreased. The cell viabilities of nanoparticles with laser treatment group started to decline at the nanoparticles concentration of 40 μM. These results

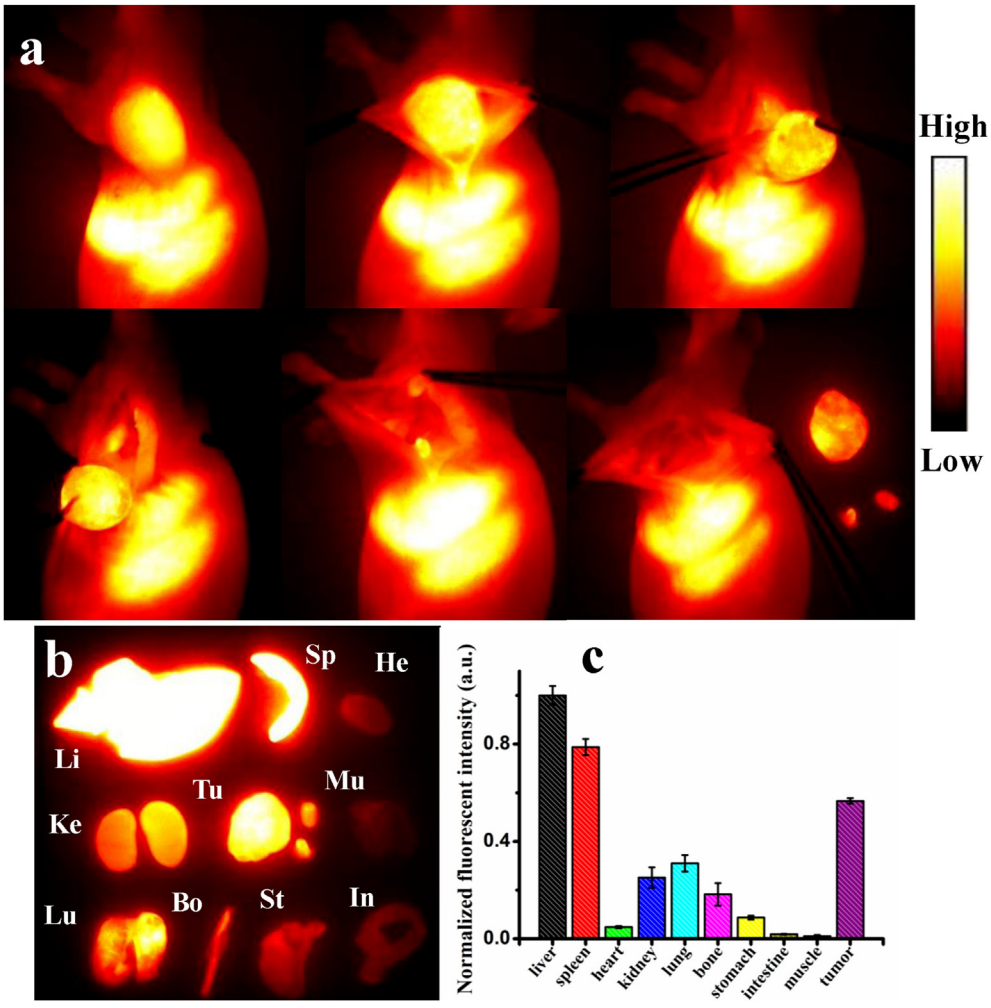

Fig. 4. NIR-II image-guided tumor surgery and biodistribution of IR1061@HSA nanoparticles *in vivo*. (a) Series images of the entire surgical process under NIR-II imaging 10 h after IR1061@HSA nanoparticle injection of 143B osteosarcoma tumor-bearing mice, including skin opening, tumor exposure, partial tumor resection, and residual tumor removal (1000 ms, 1000 LP). (b) *Ex vivo* NIR-II images (1000 ms, 1000 LP) of dissected tumors and major organs (heart, lung, liver, spleen, kidney, stomach, intestine, bone, and muscle). (c) Semiquantitative analysis of the distribution of IR1061@HSA nanoparticles according to the fluorescence intensity.

demonstrated that IR1061@HSA nanoparticles display high toxicity to tumor cells when exposed to NIR irradiation.

3.5. NIR-II imaging for assessment blood supply network of the tumor

In order to visualize the blood supply system within the tumor, IR1061@HSA nanoparticles were intravenously injected into the 143B osteosarcoma tumor-bearing nude mice (n = 3), and NIR-II images were taken to observe the main blood vessels and its accompanying branch of the tumor from multiple angles (Fig. 2a–c). The resolutions of the thickened and twisted tumor blood vessels were quantitatively analyzed using the SNR and FWHM, which ranged from 1.55 to 2.81 and from 442 μm to 578 μm (Fig. 2d–f). The observed tumor blood supply system in the NIR-II images demonstrated that IR1061@HSA nanoparticles fluorescence imaging is a promising tool for visual monitoring of tumor blood vessels with high temporal and spatial resolution [26]. The NIR-II imaging provides us with more information about tumor-feeding arteries and enables us to perform effective selective intra-arterial chemotherapy or embolization [47].

3.6. NIR-II imaging of the tumors using the IR1061@HSA nanoparticles

The feasibility of using IR1061@HSA nanoparticles for NIR-II imaging of tumors was studied in nude mice carrying 143B osteosarcoma tumors (n = 3). NIR-II imaging was performed at different time points from 1 h to 64 h after injection of IR1061@HSA nanoparticles. The tumors were clearly depicted under NIR II imaging (Fig. 3a). The tumor-to-background (T/B) ratios of the tumor images were analyzed, in which fluorescence intensity of the hip site was used as the background signal. The T/B ratio kept increasing (6.5) up to 64 h (Fig. 3b). The EPR effect and SPARC is believed to be responsible for the accumulation of IR1061@HSA nanoparticles in the tumors. As we can see from the images, the nanoparticles cleared slowly from the liver and spleen mononuclear phagocytic system, future work is required to improve the specificity and rapid clearance of this material. Since HSA has been widely used as a drug delivery vehicle, the NIR-II imaging multifunctional platform based on HSA has broad prospects, especially in image-guided surgery.

3.7. NIR-II image-guided tumor surgery using IR1061@HSA nanoparticles

After the tumors were clearly displayed with IR1061@HSA nanoparticles, the 143B osteosarcoma tumor-bearing nude mice (n = 3) were subjected to tumor resection under the guidance of NIR-II imaging. Under the real-time NIR-II imaging, multiple resections were performed, and the tumor was completely removed. NIR-II imaging shows no residual tumor (Fig. 4a). Ex vivo NIR II imaging was performed on the dissected tumors and organs to further evaluate the biodistribution of IR1061@HSA nanoparticles (Fig. 4b). In addition to the high NIR-II fluorescence intensity shown in tumors, a large number of nanoparticles were also found in the liver and spleen, indicating the possible excretion pathways of the nanoparticles (Fig. 4c). Real-time intraoperative guidance using fluorescence imaging is essential for safe and complete tumor surgery [48]. By using IR1061@HSA nanoparticles, NIR-II imaging allowed us to specifically detect osteosarcoma tumors and further demonstrated the feasibility of real-time imaging-guided tumor resection.

3.8. In vivo NIR PTT of IR1061@HSA nanoparticles

In order to evaluate the photothermal effect of IR1061@HSA nanoparticles *in vivo*, 143B osteosarcoma tumor-bearing mice (n = 3) were exposed to 808 nm wavelength laser irradiation (1 W/cm2) for 5 min 4 h after intravenously injection of nanoparticles. A visual IR thermometer was used to record the temperature changes of tumor-bearing mice treated with IR1061@HSA nanoparticles or PBS. As shown in Fig. 5a, after laser irradiation, the temperature in the tumor increased greatly with the irradiation time. In the IR1061@HSA nanoparticles group, the temperature rose and reached near 53 °C with an increase of 18 °C after laser irradiation for 5 min. On the other hand, an increase of only 5 °C up

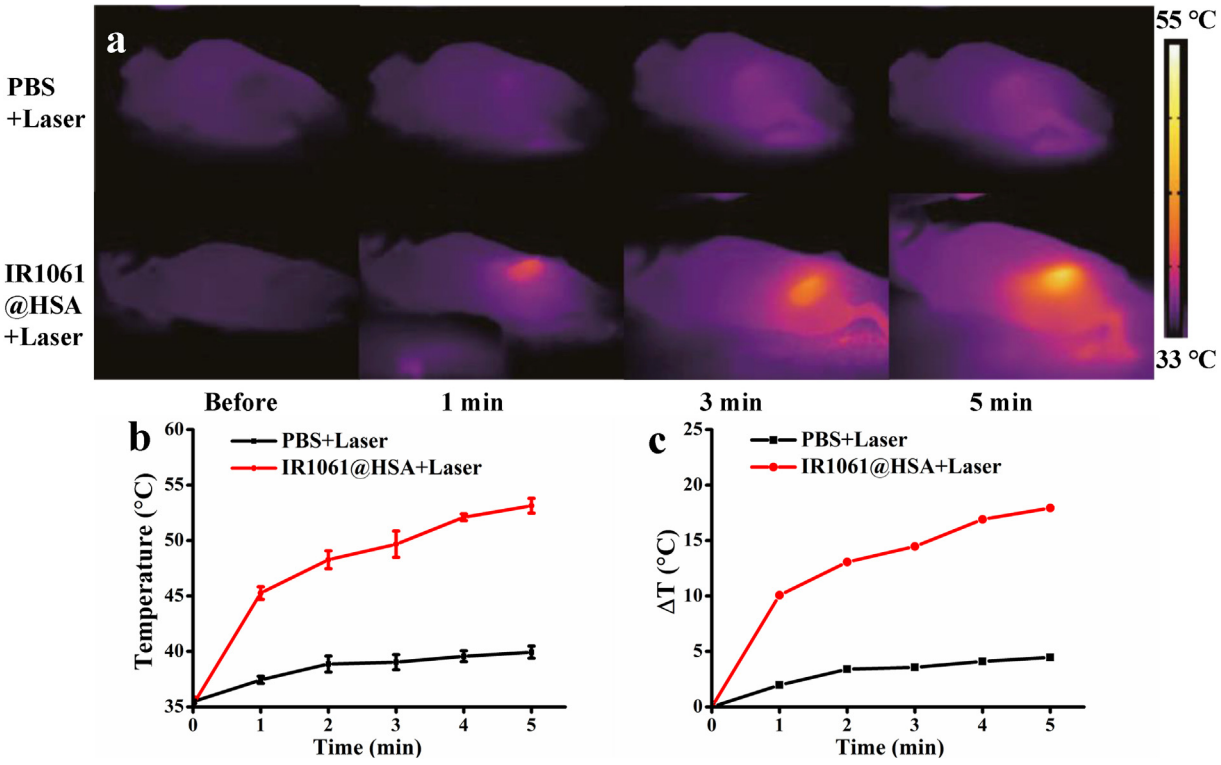

Fig. 5. *In vivo* NIR PTT of IR1061@HSA nanoparticles (a) Thermal images of 143B osteosarcoma tumor-bearing mice treated with IR1061@HSA nanoparticles or PBS at different illuminating times. (b, c) Temperature and its change (△T) of the tumor in the control and experimental group.

to 40 °C in the PBS group (Fig. 5b and c). These results indicated that IR1061@HSA nanoparticles produce thermal effect to ensure it to be a promising photothermal agent *in vivo*.

3.9. PTT efficacy of IR1061@HSA nanoparticles in vivo

In order to evaluate the phototherapy efficacy of IR1061@HSA nanoparticles *in vivo*, an anti-tumor studies were conducted. When the tumor diameters reached ~1 cm, 143B osteosarcoma tumor-bearing mice (n = 5) were intravenously injected with IR1061@HSA nanoparticles or PBS. As shown in Fig. 6a, after 808 nm wavelength laser irradiation, the tumors of mice treated with IR1061@HSA nanoparticles decline significantly and almost disappear on the 15th day. The scar tissues gradually healed during those days. However, in the other three groups (PBS, PBS plus laser, and IR1061@HSA nanoparticles only), the volumes of tumors greatly increased on day 15 compared with the baseline (Fig. 6c). There was no significant change in body weight among groups (Fig. 6b). These results demonstrated that IR1061@HSA nanoparticles exhibit phototherapeutic efficacy in suppressing tumor growth. No abnormality was found in the stained images of major organ slices with Hematoxylin and eosin (Fig. S6). IR1061@HSA nanoparticles irradiated with lower laser energy of 1 W/cm^2 were sufficient for PTT. IR1061@HSA nanoparticles were proven to have a strong photothermal conversion effect. The optimized NIR-II image-guided PTT completely cured the 143B osteosarcoma tumor-bearing mice. IR1061@HSA nanoparticles showed broad prospects in tumor PTT guided by NIR-II fluorescence images, especially in phototheranostics for osteosarcoma. As IR1061 has the NIR-II absorption spectrum, so it has the potential for deep tumor photothermal treatment with 1064 nm laser [49].

Last and most important, the first-in-human study of NIR-II imaging in patients demonstrated the feasibility of intraoperative NIR-II image-guided surgery in the clinic practice [50]. In addition, the clinical use of nab-paclitaxel proved the great potential of albumin-based nab technology [30]. Overall, the success of these NIR-II technologies and nanomedicines ensures the clinical application prospects of the albumin-NIR II dye IR1061@ HSA nanoparticles, making it a versatile cancer phototheranostics platform.

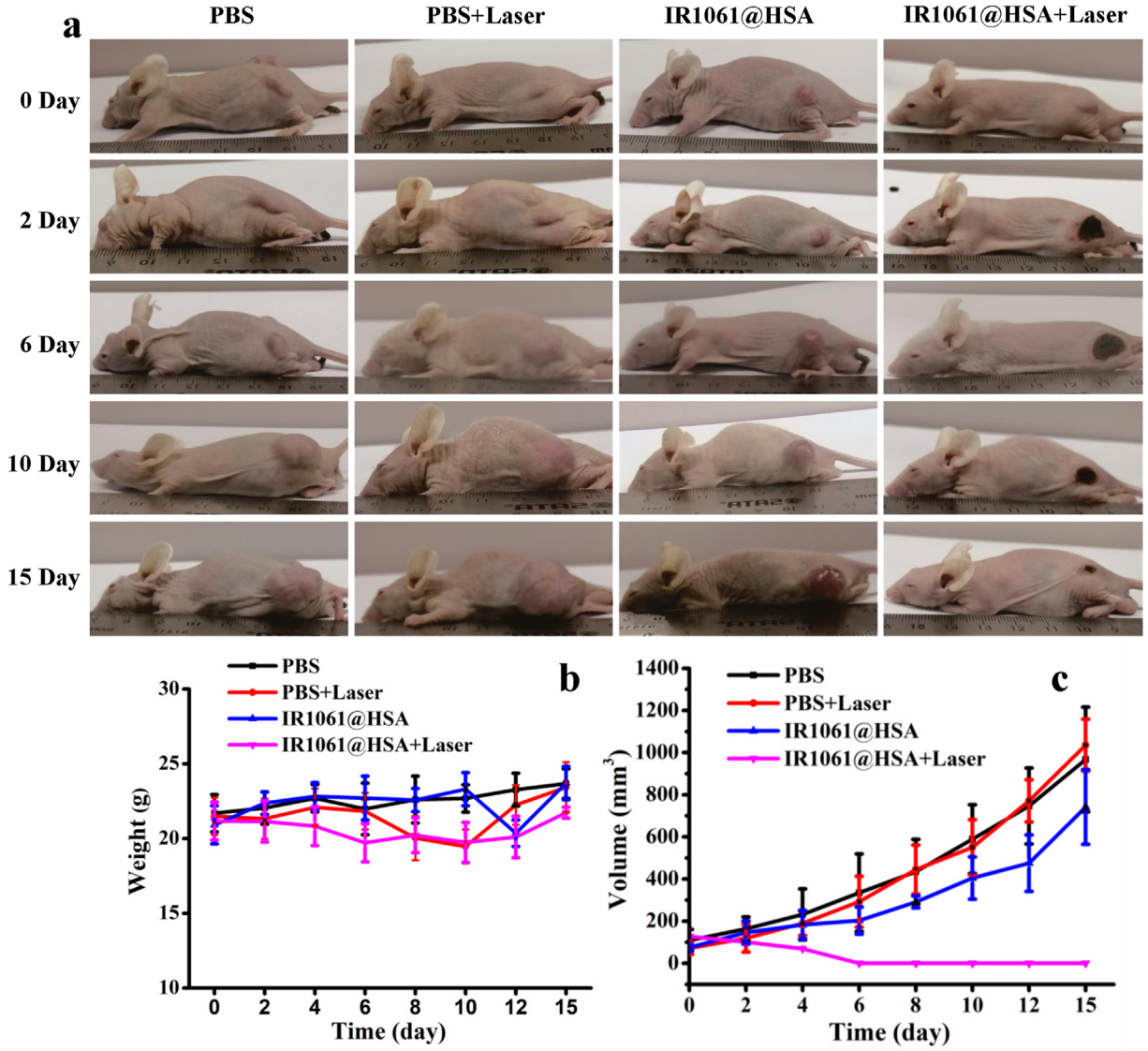

Fig. 6. PTT efficacy of IR1061@HSA nanoparticles *in vivo*. (a) Photographs of 143B osteosarcoma tumor-bearing mice in different treatment groups. (b, c) Curves of body weight change and tumor growth of mice over time in different treatment groups.

4. Conclusions

The novel J-aggregates IR1061@HSA nanoparticles have been successfully developed and effectively used for *in vivo* NIR-II imaging to noninvasively visualize and monitor the tumor vascular networks, as well as real-time NIR-II image-guided intraoperative tumor resection. Moreover, IR1061@HSA nanoparticles have a strong photothermal conversion effect and could thus be an ideal photothermal agent for cancer PTT. Overall, IR1061@HSA, as an albumin-based NIR II dye nanoparticle with high biocompatibility, provides an integrated versatile platform for cancer phototheranostics with promising clinical translation prospects.

Credit author statement

Bulin Du: Conceptualization, Methodology, Investigation, Writing–original draft. Ruiqi Liu: Conceptualization, Methodology, Investigation, Writing–original draft. Chunrong Qu: Conceptualization, Methodology. Kun Qian: Software, Validation. Yongkuan Suo: Investigation. Fengxia Wu: Investigation. Hongda Chen: Investigation. Xuena Li: Validation. Yaming Li: Supervision, Funding acquisition. Hongguang Li: Supervision, Writing- Reviewing and Editing. Zhen Cheng: Supervision, Writing- Reviewing and Editing.

Data availability statement

The data sets used and/or analyzed during the current study are available from the corresponding author on reasonable request.

Declaration of competing interest

The authors declare that they have no known competing financial interests or personal relationships that could have appeared to influence the work reported in this paper.

Acknowledgements

This work was partially supported by the Department of Radiology, Stanford University, and National Natural Science Foundation of China (82171987, 81971652 and 81761148029).

Appendix A. Supplementary data

Supplementary data to this article can be found online at https://doi.org/10.1016/j.mtbio.2022.100366.

References

[1] H. Sung, J. Ferlay, R.L. Siegel, M. Laversanne, I. Soerjomataram, A. Jemal, F. Bray, Global cancer statistics 2020: GLOBOCAN estimates of incidence and mortality worldwide for 36 cancers in 185 countries, Ca - Cancer J. Clin. 71 (2021) 209–249, https://doi.org/10.3322/caac.21660.

[2] Y. Cai, X. Chen, J. Si, X. Mou, X. Dong, All-in-One nanomedicine: multifunctional single-component nanoparticles for cancer theranostics, Small 17 (2021), e2103072, https://doi.org/10.1002/smll.202103072.

[3] G. Feng, G.-Q. Zhang, D. Ding, Design of superior phototheranostic agents guided by Jablonski diagrams, Chem. Soc. Rev. 49 (2020) 8179–8234, https://doi.org/10.1039/d0cs00671h.

[4] Z. Zhang, M. Kang, H. Tan, N. Song, M. Li, P. Xiao, D. Yan, L. Zhang, D. Wang, B.Z. Tang, The fast-growing field of photo-driven theranostics based on aggregation-induced emission, Chem. Soc. Rev. 51 (2022), https://doi.org/10.1039/d1cs01138c, 1983–2030.

[5] Y. Cai, W. Si, W. Huang, P. Chen, J. Shao, X. Dong, Organic dye based nanoparticles for cancer phototheranostics, Small 14 (2018), e1704247, https://doi.org/10.1002/smll.201704247.

[6] H. Chen, K. Shou, S. Chen, C. Qu, Z. Wang, L. Jiang, M. Zhu, B. Ding, K. Qian, A. Ji, H. Lou, L. Tong, A. Hsu, Y. Wang, D.W. Felsher, Z. Hu, J. Tian, Z. Cheng, Smart self-assembly amphiphilic cyclopeptide-dye for near-infrared window-II imaging, Adv. Mater. 33 (2021), e2006902, https://doi.org/10.1002/adma.202006902.

[7] H. Lou, A. Ji, C. Qu, S. Duan, H. Liu, H. Chen, Z. Cheng, A novel NIR-II nanoprobe for precision imaging of micro-meter sized tumor metastases of multi-organs and skin flap, Chem. Eng. J. 449 (2022), 137848, https://doi.org/10.1016/j.cej.2022.137848.

[8] A. Ji, H. Lou, C. Qu, W. Lu, Y. Hao, J. Li, Y. Wu, T. Chang, H. Chen, Z. Cheng, Acceptor engineering for NIR-II dyes with high photochemical and biomedical performance, Nat. Commun. 13 (2022) 3815, https://doi.org/10.1038/s41467-022-31521-y.

[9] L. Li, X. Dong, J. Li, J. Wei, A short review on NIR-II organic small molecule dyes, Dyes Pigments 183 (2020), 108756, https://doi.org/10.1016/J.DYEPIG.2020.108756.

[10] A.L. Antaris, H. Chen, K. Cheng, Y. Sun, G. Hong, C. Qu, S. Diao, Z. Deng, X. Hu, B. Zhang, X. Zhang, O.K. Yaghi, Z.R. Alamparambil, X. Hong, Z. Cheng, H. Dai, A small-molecule dye for NIR-II imaging, Nat. Mater. 15 (2016) 235–242, https://doi.org/10.1038/nmat4476.

[11] B. Chang, D. Li, Y. Ren, C. Qu, X. Shi, R. Liu, H. Liu, J. Tian, Z. Hu, T. Sun, Z. Cheng, A phosphorescent probe for in vivo imaging in the second near-infrared window, Nat. Biomed. Eng. 6 (2022) 629–639, https://doi.org/10.1038/s41551-021-00773-2.

[12] B. Ding, Y. Xiao, H. Zhou, X. Zhang, C. Qu, F. Xu, Z. Deng, Z. Cheng, X. Hong, Polymethine thiopyrylium fluorophores with absorption beyond 1000 nm for biological imaging in the second near-infrared subwindow, J. Med. Chem. 62 (2019) 2049–2059, https://doi.org/10.1021/acs.jmedchem.8b01682.

[13] Y. Du, X. Liu, S. Zhu, Near-infrared-II cyanine/polymethine dyes, current state and perspective, Front. Chem. 9 (2021), 718709, https://doi.org/10.3389/fchem.2021.718709.

[14] Z. Tao, G. Hong, C. Shinji, C. Chen, S. Diao, A.L. Antaris, B. Zhang, Y. Zou, H. Dai, Biological imaging using nanoparticles of small organic molecules with fluorescence emission at wavelengths longer than 1000 nm, Angew. Chem., Int. Ed. Engl. 52 (2013) 13002–13006, https://doi.org/10.1002/anie.201307346.

[15] M. Umezawa, M. Haruki, M. Yoshida, M. Kamimura, K. Soga, Effects of processing pH on emission intensity of over-1000 nm near-infrared fluorescence of dye-loaded polymer micelle with polystyrene core, Anal. Sci. 37 (2021) 485–490, https://doi.org/10.2116/analsci.20SCP09.

[16] Q. Chen, J. Chen, M. He, Y. Bai, H. Yan, N. Zeng, F. Liu, S. Wen, L. Song, Z. Sheng, C. Liu, C. Fang, Novel small molecular dye-loaded lipid nanoparticles with efficient near-infrared-II absorption for photoacoustic imaging and photothermal therapy of hepatocellular carcinoma, Biomater. Sci. 7 (2019) 3165–3177, https://doi.org/10.1039/c9bm00528e.

[17] X. Xie, Y. Hu, C. Zhang, J. Song, S. Zhuang, Y. Wang, A targeted biocompatible organic nanoprobe for photoacoustic and near-infrared-II fluorescence imaging in living mice, RSC Adv. 9 (2018) 301–306, https://doi.org/10.1039/C8RA08163H.

[18] Y. Tang, Y. Li, X. Hu, H. Zhao, Y. Ji, L. Chen, W. Hu, W. Zhang, X. Li, X. Lu, W. Huang, Q. Fan, Dual lock-and-key"-controlled nanoprobes for ultrahigh specific fluorescence imaging in the second near-infrared window, Adv. Mater. 30 (2018), e1801140, https://doi.org/10.1002/adma.201801140.

[19] Q. Chen, Z. Liu, Albumin carriers for cancer theranostics: a conventional platform with new promise, Adv. Mater. 28 (2016) 10557–10566, https://doi.org/10.1002/adma.201600038.

[20] S. Zhang, W.J. Cho, A.T. Jin, L.Y. Kok, Y. Shi, D.E. Heller, Y.-A.L. Lee, Y. Zhou, X. Xie, J.R. Korzenik, J.K. Lennerz, G. Traverso, Heparin-Coated albumin nanoparticles for drug combination in targeting inflamed intestine, Adv. Healthc. Mater. 9 (2020), e2000536, https://doi.org/10.1002/adhm.202000536.

[21] J.V. Gregory, P. Kadiyala, R. Doherty, M. Cadena, S. Habeel, E. Ruoslahti, P.R. Lowenstein, M.G. Castro, J. Lahann, Systemic brain tumor delivery of synthetic protein nanoparticles for glioblastoma therapy, Nat. Commun. 11 (2020) 5687, https://doi.org/10.1038/s41467-020-19225-7.

[22] A.M. Merlot, D.S. Kalinowski, R. Des Richardson, Unraveling the mysteries of serum albumin-more than just a serum protein, Front. Physiol. 5 (2014) 299, https://doi.org/10.3389/fphys.2014.00299.

[23] C.R. Park, J.H. Jo, M.G. Song, J.Y. Park, Y.-H. Kim, H. Youn, S.H. Paek, J.-K. Chung, J.M. Jeong, Y.-S. Lee, K.W. Kang, Secreted protein acidic and rich in cysteine mediates active targeting of human serum albumin in U87MG xenograft mouse models, Theranostics 9 (2019) 7447–7457, https://doi.org/10.7150/thno.34883.

[24] Y. Zhang, Y. Wan, Y. Chen, N.T. Blum, J. Lin, P. Huang, Ultrasound-enhanced chemo-photodynamic combination therapy by using albumin "Nanoglue"-Based nanotheranostics, ACS Nano 14 (2020) 5560–5569, https://doi.org/10.1021/acsnano.9b09827.

[25] X. Chai, H.-H. Han, A.C. Sedgwick, N. Li, Y. Zang, T.D. James, J. Zhang, X.-L. Hu, Y. Yu, Y. Li, Y. Wang, J. Li, X.-P. He, H. Tian, A photochromic fluorescent probe strategy for the super-resolution imaging of biologically important biomarkers, J. Am. Chem. Soc. (2020) 18005–18013, https://doi.org/10.1021/jacs.0c05379.

[26] B. Du, C. Qu, K. Qian, Y. Ren, Y. Li, X. Cui, S. He, Y. Wu, T. Ko, R. Liu, X. Li, Y. Li, Z. Cheng, An IR820 dye-protein complex for second near-infrared window and photoacoustic imaging, Adv. Opt. Mater. 8 (2020), 1901471, https://doi.org/10.1002/adom.201901471.

[27] A.L. Antaris, H. Chen, S. Diao, Z. Ma, Z. Zhang, S. Zhu, J. Wang, A.X. Lozano, Q. Fan, L. Chew, M. Zhu, K. Cheng, X. Hong, H. Dai, Z. Cheng, A high quantum yield molecule-protein complex fluorophore for near-infrared II imaging, Nat. Commun. 8 (2017), 15269, https://doi.org/10.1038/ncomms15269.

[28] Q. Chen, C. Wang, Z. Zhan, W. He, Z. Cheng, Y. Li, Z. Liu, Near-infrared dye bound albumin with separated imaging and therapy wavelength channels for imaging-guided photothermal therapy, Biomaterials 35 (2014) 8206–8214, https://doi.org/10.1016/j.biomaterials.2014.06.013.

[29] N.C. Stein, D. Mulac, J. Fabian, F.C. Herrmann, K. Langer, Nanoparticle albumin-bound mTHPC for photodynamic therapy: preparation and comprehensive characterization of a promising drug delivery system, Int. J. Pharm. 582 (2020), 119347, https://doi.org/10.1016/j.ijpharm.2020.119347.

[30] Q. Fu, J. Sun, W. Zhang, X. Sui, Z. Yan, Z. He, Nanoparticle albumin-bound (NAB) technology is a promising method for anti-cancer drug delivery, Recent Pat. Anti-

Cancer Drug Discov. https://doi.org/10.2174/157489209789206869, 2009, 4-262-272.
[31] P.T.T. Pham, X.T. Le, H. Kim, H.K. Kim, E.S. Lee, K.T. Oh, H.-G. Choi, Y.S. Youn, Indocyanine green and curcumin Co-loaded nano-fireball-like albumin nanoparticles based on near-infrared-induced hyperthermia for tumor ablation, Int. J. Nanomed. 15 (2020) 6469–6484, https://doi.org/10.2147/IJN.S262690.
[32] S. Gao, G. Wei, S. Zhang, B. Zheng, J. Xu, G. Chen, M. Li, S. Song, W. Fu, Z. Xiao, W. Lu, Albumin tailoring fluorescence and photothermal conversion effect of near-infrared-II fluorophore with aggregation-induced emission characteristics, Nat. Commun. 10 (2019) 2206, https://doi.org/10.1038/s41467-019-10056-9.
[33] C. Jiang, H. Cheng, A. Yuan, X. Tang, J. Wu, Y. Hu, Hydrophobic IR780 encapsulated in biodegradable human serum albumin nanoparticles for photothermal and photodynamic therapy, Acta Biomater. 14 (2015) 61–69, https://doi.org/10.1016/j.actbio.2014.11.041.
[34] S. Cohen, M. Pellach, Y. Kam, I. Grinberg, E. Corem-Salkmon, A. Rubinstein, S. Margel, Synthesis and characterization of near IR fluorescent albumin nanoparticles for optical detection of colon cancer, Mater. Sci. Eng. C, Mater. Biol. 33 (2013) 923–931, https://doi.org/10.1016/j.msec.2012.11.022.
[35] I.M. Steinhauser, K. Langer, K.M. Strebhardt, B. Spänkuch, Effect of trastuzumab-modified antisense oligonucleotide-loaded human serum albumin nanoparticles prepared by heat denaturation, Biomaterials 29 (2008) 4022–4028, https://doi.org/10.1016/j.biomaterials.2008.07.001.
[36] Y. Huang, N. He, Y. Wang, D. Shen, Q. Kang, R. Zhao, L. Chen, Self-assembly of nanoparticles by human serum albumin and photosensitizer for targeted near-infrared emission fluorescence imaging and effective phototherapy of cancer, J. Mater. Chem. B 7 (2019) 1149–1159, https://doi.org/10.1039/C8TB03054E.
[37] D. Zhao, X. Zhao, Y. Zu, J. Li, Y. Zhang, R. Jiang, Z. Zhang, Preparation, characterization, and in vitro targeted delivery of folate-decorated paclitaxel-loaded bovine serum albumin nanoparticles, Int. J. Nanomed. 5 (2010) 669–677, https://doi.org/10.2147/ijn.s12918.
[38] J. Yang, S. He, Z. Hu, Z. Zhang, C. Cao, Z. Cheng, C. Fang, J. Tian, In vivo multifunctional fluorescence imaging using liposome-coated lanthanide nanoparticles in near-infrared-II/IIa/IIb windows, Nano Today 38 (2021), 101120, https://doi.org/10.1016/j.nantod.2021.101120.
[39] L. Li, Z. Zeng, Z. Chen, R. Gao, L. Pan, J. Deng, X. Ye, J. Zhang, S. Zhang, C. Mei, J. Yu, Y. Feng, Q. Wang, A.-Y. Yu, M. Yang, J. Huang, Microenvironment-triggered degradable hydrogel for imaging diagnosis and combined treatment of intraocular choroidal melanoma, ACS Nano 14 (2020) 15403–15416, https://doi.org/10.1021/acsnano.0c06000.
[40] B. von Storp, A. Engel, A. Boeker, M. Ploeger, K. Langer, Albumin nanoparticles with predictable size by desolvation procedure, J. Microencapsul. 29 (2012) 138–146, https://doi.org/10.3109/02652048.2011.635218.
[41] C. Weber, C. Coester, J. Kreuter, K. Langer, Desolvation process and surface characterisation of protein nanoparticles, Int. J. Pharm. 194, Int. J. Pharm. 194 (1) (2000) 91–102, https://doi.org/10.1016/S0378-5173(99)00370-1, 91–102.
[42] H. Piwoński, S. Nozue, H. Fujita, T. Michinobu, S. Habuchi, Organic J-aggregate nanodots with enhanced light absorption and near-unity fluorescence quantum yield, Nano Lett. 21 (2021) 2840–2847, https://doi.org/10.1021/acs.nanolett.0c04928.
[43] J. Xia, Z. Li, Z. Xie, M. Zheng, Near-Infrared absorbing J-Aggregates of boron dipyrromethene for high efficient photothermal therapy, J. Colloid Interface Sci. 599 (2021) 476–483, https://doi.org/10.1016/j.jcis.2021.04.086.
[44] W. Chen, C.-A. Cheng, E.D. Cosco, S. Ramakrishnan, J.G.P. Lingg, O.T. Bruns, J.I. Zink, E.M. Sletten, Shortwave infrared imaging with J-aggregates stabilized in hollow mesoporous silica nanoparticles, J. Am. Chem. Soc. 141 (2019) 12475–12480, https://doi.org/10.1021/jacs.9b05195.
[45] J.H. Kim, T. Schembri, D. Bialas, M. Stolte, F. Würthner, Slip-stacked J-aggregate materials for organic solar cells and photodetectors, Adv. Mater. (2021), e2104678, https://doi.org/10.1002/adma.202104678.
[46] M. Su, Q. Han, X. Yan, Y. Liu, P. Luo, W. Zhai, Q. Zhang, L. Li, C. Li, A supramolecular strategy to engineering a non-photobleaching and near-infrared absorbing nano-J-aggregate for efficient photothermal therapy, ACS Nano 15 (2021) 5032–5042, https://doi.org/10.1021/acsnano.0c09993.
[47] S. Ohba, J. Yokoyama, M. Fujimaki, S. Ito, M. Kojima, K. Shimoji, K. Ikeda, Significant improvement in superselective intra-arterial chemotherapy for oral cancer by using indocyanine green fluorescence, Oral Oncol. 48 (2012) 1101–1105, https://doi.org/10.1016/j.oraloncology.2012.08.007.
[48] S. Hernot, L. van Manen, P. Debie, J.S.D. Mieog, A.L. Vahrmeijer, Latest developments in molecular tracers for fluorescence image-guided cancer surgery, Lancet Oncol. 20 (2019) e354–e367, https://doi.org/10.1016/S1470-2045(19)30317-1.
[49] X. Wu, Y. Suo, H. Shi, R. Liu, F. Wu, T. Wang, L. Ma, H. Liu, Z. Cheng, Deep-tissue photothermal therapy using laser illumination at NIR-IIa window, Nano-Micro Lett. 12 (2020) 38, https://doi.org/10.1007/s40820-020-0378-6.
[50] Z. Hu, C. Fang, B. Li, Z. Zhang, C. Cao, M. Cai, S. Su, X. Sun, X. Shi, C. Li, T. Zhou, Y. Zhang, C. Chi, P. He, X. Xia, Y. Chen, S.S. Gambhir, Z. Cheng, J. Tian, First-in-human liver-tumour surgery guided by multispectral fluorescence imaging in the visible and near-infrared-I/II windows, Nat. Biomed. Eng. 4 (2020) 259–271, https://doi.org/10.1038/s41551-019-0494-0.